Electrophoretic deposition of nanocrystalline hydroxyapatite on Ti6Al4V/TiO$_2$ substrate

**Prateek Jain, Tapendu Mandal, Prem Prakash,
Ashish Garg, Kantesh Balani**

Abstract Hydroxyapatite is a bioactive material that is the main inorganic constituent of human hard tissue (Ca/P ratio of 1.67) whose coatings provide requisite surface bioactivity to the bone implants. In the current work, the characteristics of nanocrystalline hydroxyapatite (HA) coatings, electrophoretically deposited on Ti6Al4V substrate, have been investigated. To enhance the coating's compatibility, a 0.75 μm thick TiO$_2$ layer was thermally grown as a diffusion barrier prior to electrophoretic deposition of HA. Subsequently, HA was electrophoretically deposited (EPD) at different deposition voltages (100–250 V) while keeping the deposition time as 10 s. Both anodic oxidation during EPD for 10 s and thermal oxidation during sintering at 1000°C for 2 h resulted in the growth of a TiO$_2$ layer thickness of more than 25 μm. Enhancement of voltage also has shown significant influence on the mechanism of the evolution of biphasic microstructures, attributed to the simultaneous growth of TiO$_2$ and HA phases. Optimized distribution of HA and TiO$_2$ phases was evidenced at 200 V, with explicit HA retention as observed via transmission electron microscopy. An empirical relationship is developed to relate the voltage with the suppression of cracking in the deposited coatings.

Keywords Electrophoretic deposition, Hydroxyapatite, Coatings, Nanocrystalline, Titanium dioxide

P. Jain, T. Mandal, A. Garg, K. Balani (✉)
Department of Materials Science and Engineering, Indian Institute of Technology Kanpur, Kanpur 208016, India
e-mail: kbalani@iitk.ac.in

T. Mandal, P. Prakash
Cenogen Materials Pvt. Ltd., SIIC, Indian Institute of Technology Kanpur, Kanpur 208016, India

Introduction

Hydroxyapatite, Ca$_{10}$(PO$_4$)$_6$(OH)$_2$, is one of the most popular bioceramic materials, possessing desired levels of bioactivity which are needed for biomedical applications.[1] Due to near-similar chemical composition (Ca/P ratio of 1.67) and high biocompatibility with natural bone tissue as well as a very close proximity to apatite, a bone mineral, it has been widely used in medical and dental applications.[2] However, it cannot be used directly as a structural material due to its poor fracture toughness (<1 MPa m$^{1/2}$) since all structural bioimplants must possess a load bearing capability.[3] While metals and alloys (e.g., titanium, stainless steel) can provide better bonding strength (∼20 MPa for Ti-6Al-4V)[4,5] to orthopedic implants, these show inferior bioactivity, which is a necessity for biomedical applications.[5] To retain excellent mechanical performance of bioimplants while achieving enhanced cyto-compatibility, the idea of coating metal/alloy with HA has been synergistically adopted.[6] Poor mechanical properties of HA such as low fracture toughness, tribological, and fatigue properties can also be enhanced by (i) films on alloys,[7] and (ii) composites such as reinforcement of HA with YSZ (yttria-stabilized zirconia), Al$_2$O$_3$ (alumina), and CNT (carbon nanotubes).[8–10]

There are many coating techniques available for depositing HA on metal substrates, such as electrophoresis,[11–14] chemical electrodeposition,[15] dip coating,[16] plasma spraying,[17,18] pulse laser deposition,[6] solution gel,[19,20] sputter coating, biomimetric coating,[21] and electrostatic spraying.[22] While each coating technique has its own advantages and limitations, electrophoretic deposition (EPD) exhibits a strong capability to form complex shapes and patterns while providing a high degree of control over microscopic and macroscopic properties. More importantly, in contrast to most physical vapor and chemical deposition processes, the level of porosity required in the HA films can easily

be achieved using EPD. The morphology of HA coatings can be altered by adjusting deposition parameters like voltage, time, and powder size.[12,23–25]

One of the major issues with HA coating on a metallic substrate (like Ti6Al4V) has been its poor adhesion to the substrate (∼13.8 MPa)[26] and subsequent crack formation because of a weak metal/ceramic interface.[27] These cracks originate as a result of shrinkage during sintering in dry coatings.[26,28] With most post-sintered HA coating, while sintering enhances the strength and densification of the deposited HA coating, it also leads to increased HA decomposition. The latter is highly detrimental for the biological environment as it enhances the in-vitro dissolution.[14,29] Though pure HA is chemically stable up to 1200°C, it can decompose into tri-calcium phosphate, $Ca_3(PO_4)_2$ at much lower temperature, ∼950°C or so, when heated on a metallic substrate due to migration of the metal ions.[28,30]

In this regard, the use of intermediate barrier layers between HA and the substrate has been shown to reduce HA decomposition by restricting the diffusion of metal ions from the substrate into the HA coating. For instance, Wei et al. used an extra inner diffusion barrier layer of HA,[19,29] reducing the decomposition of the top layer, though filling of cracks in the inner layers by the outer layer led to a deteriorated adhesion strength of coating. To improve the adhesion strength and obtain a dense crack-free surface of the coatings, researchers[31,32] have shown that the use of dense titanium oxide (TiO_2) film as a barrier layer between Ti alloy (Ti6Al4V) substrate and HA coating provides a very good combination of bioactivity, chemical stability, and mechanical integrity. A few other reports also showed that TiO_2 barrier film enhances both the corrosion resistance and the biocompatibility of Ti6Al4V.[33,34]

EPD is a process which can lead to the formation of macroporous HA possessing similar microstructural morphology as that of apatite found in the human bone. However, the selection of a submicron sized range of HA particles for the deposition is critical as EPD deposition of these particles requires high voltage to impart a critical velocity enough to get these particles attached to the substrate.[35] It has been reported that while the coatings fabricated at a constant low voltage

(∼20 V) produce high bond strength on Ti substrates they show low biocompatibility.[36] On the other hand, the coatings obtained at a high voltage (∼200 V) yield a comparatively inferior adhesion to Ti substrates, but exhibit satisfactory osteoinduction to bone.[36] Although these and other past studies emphasize the utility of TiO_2 as an intermediate layer to improve the utility of HA coating, the microstructure development of these coatings has been poorly understood. From the perspective of developing a macroporous coating with sufficient adhesion as well as bioactivity, it is very important to understand how the microstructure in the coating develops and this is the basis of the current work.

In the current work, a transition layer of thermally grown titanium oxide is intentionally grown between Ti6Al4V and EPD grown HA coating to prevent HA decomposition due to ionic transport from metallic substrate to HA.[14,29] The presence of a TiO_2 layer also introduces ceramic–ceramic (TiO_2–HA) interface in place of metal–ceramic (Ti6Al4V/HA) interface, hence reducing the thermal expansion coefficient mismatch between the coating and substrate.[26] Herein, thin and porous HA coatings were deposited by EPD with submicron HA particles for a set of deposition voltages between 100 and 250 V, and were subsequently sintered at 1000°C for 2 h in nitrogen atmosphere in order to observe the effect of deposition voltage. Microscopy investigations reveal a biphasic microstructure with island boundaries with dense, faceted crystalline structures of TiO_2 along the highly porous islands of HA.

Experimental

The sequence of the stepwise processes and formation of different layers is demonstrated in the schematic shown in Fig. 1 and described in the following section.

Powder production

Nanocrystalline HA powder synthesized through dry mechano-chemical method (purity 98%+, Cenogen
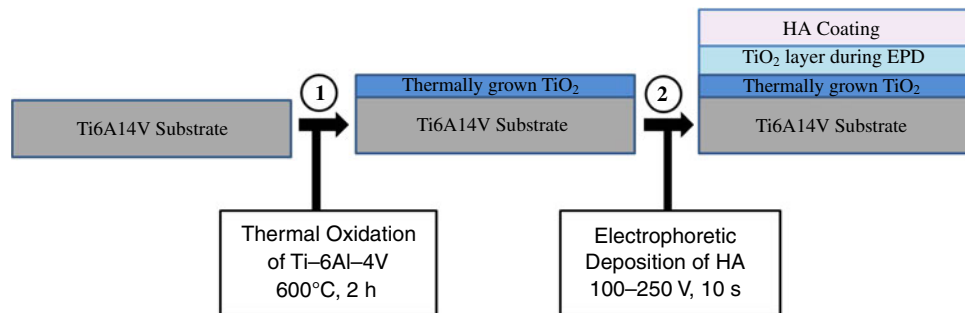

Fig. 1: Schematic diagram of the stepwise progress of samples with different experimental steps

Materials, Patent Application No. 828/DEL/2008) in a specially designed high-energy dual-drive planetary mill was used for the EPD deposition of the HA coatings. An average crystallite size of 15 nm and a median particle size of 1.1 μm were estimated by X-ray diffraction (XRD) analysis and laser particle analyzer, respectively.

Substrate preparation

Flat samples of Ti6Al4V were polished to mirror finish and were thoroughly ultrasonicated in water bath for 30 min, followed by acetone wash. Subsequently Ti6Al4V samples were heated at 600°C for 2 h in air to yield uniform blue colored films of titanium oxide.

Electrophoretic deposition (EPD)

To prepare a suspension of EPD of HA on Ti6Al4V substrate, 5 g of nanocrystalline HA powder (in 500 mL ethanol solution) was wet ball milled (model Fritsch Pulverisette) for 5 h. The suspension was then dispersed for 30 min in an ultrasonic bath (model Fritsch Laborette), and was left overnight and sedimented particles were discarded. Finally, after separating the agglomerate, the suspension was again ultrasonically dispersed for 30 min to insure a good dispersion of the particles, which means that finer particles (<1.1 μm obtained by laser particle analyzer) were being used for EPD. The pH value of HA/ethanol suspension was adjusted to approximately 4 by adding a few drops of 1 M HCl to adjust the zeta potential of the solution.

A glass cell was used for the EPD of HA on these samples of Ti6Al4V. The electrodes were placed parallel to each other in the suspension, at a distance of ~5 cm and were connected to a DC power supply (Scientific Dc power, model no. 2341). EPD was performed at different operating voltages of 100, 150, 200, and 250 V for a fixed deposition time of 10 s. The samples were named as T100, T150, T200, and T250, respectively, as shown in Table 1.

After HA deposition on the Ti6Al4V substrates, the coatings were dried in air at room temperature for 1 h, and were then sintered in a tube furnace at 1000°C for 2 h in the nitrogen atmosphere at heating as well as cooling rate of 50°C/h.

Phase and microstructural characterization

Phase identification of the samples was done on a Thermo Electron Corporation, ARL X'TRA, X-ray diffractometer using Cu K$_\alpha$ (λ = 1.542 Å) radiation and at a scan speed of 3°/min. The crystal system and the corresponding lattice parameters were compared with the standard data file of International Centre for Diffraction Data (ICDD File nos. 89-5009, 89-4037, 65-4776, 89-6440, and 22-1058). The microstructure of coatings and its morphology were observed with a Carl Zeiss scanning electron microscope (Model EVO-50). Compositional analysis of the samples was investigated by energy dispersive spectroscopy (EDS, Oxford Instruments). Microstructure of selected samples was investigated using a 200 keV FEI-transmission electron microscope (Technai 20 U Twin TEM). Hardness of the coatings was measured by Vickers Indentation method (Bareiss Digi test' model) at load of 50 g with a dwell time of 15 s. Evaluation of the microporosity, island size and fraction of the phases present was carried out by analysis of the SEM micrographs using Image J software (Wayne Rasband National Institute of Health, USA). It should be mentioned that the use of colours in the SEM images is only to illustrate various phases clearly.

Results

Phase identification

First, XRD patterns of unoxidized Ti6Al4V substrates and oxidized substrates were obtained and the results are shown in Fig. 2a. Upon peak matching with the relevant ICDD files, the peaks corresponded to β-Ti and rutile TiO$_2$ and are indexed. Figure 2a also shows formation of rutile phase of TiO$_2$ on the Ti6Al4V substrate after the thermal oxidation of the substrates.

XRD pattern of EPD deposited and sintered HA coatings on substrates (samples T250, T200, T150, and T100) shows HA and TiO$_2$ peaks as presented in Fig. 2b and there is no major difference between samples

Table 1: Sample nomenclature and physical properties of deposited coatings

Sample	Deposition voltage (V)	Deposition time (s)	% Porosity (in HA)	Island size HA	% Phase TiO$_2$	% Phase HA	Crystallite size (nm) TiO$_2$	Crystallite size (nm) HA
T250	250	10	33.0 ± 3.2	60.0 ± 10.0	16.9 ± 1.5	83.1 ± 1.5	41	41
T200	200	10	23.7 ± 2.4	76.9 ± 15.7	19.7 ± 1.3	80.3 ± 1.3	41	41
T150	150	10	NA*	NA*	NA*	NA*	42	41
T100	100	10	21.6 ± 3.8	96.1 ± 15.9	21.8 ± 1.2	78.2 ± 1.2	42	41

*For sample T150, island size and % phase estimation was not feasible due to their unclear morphology and incomplete coverage
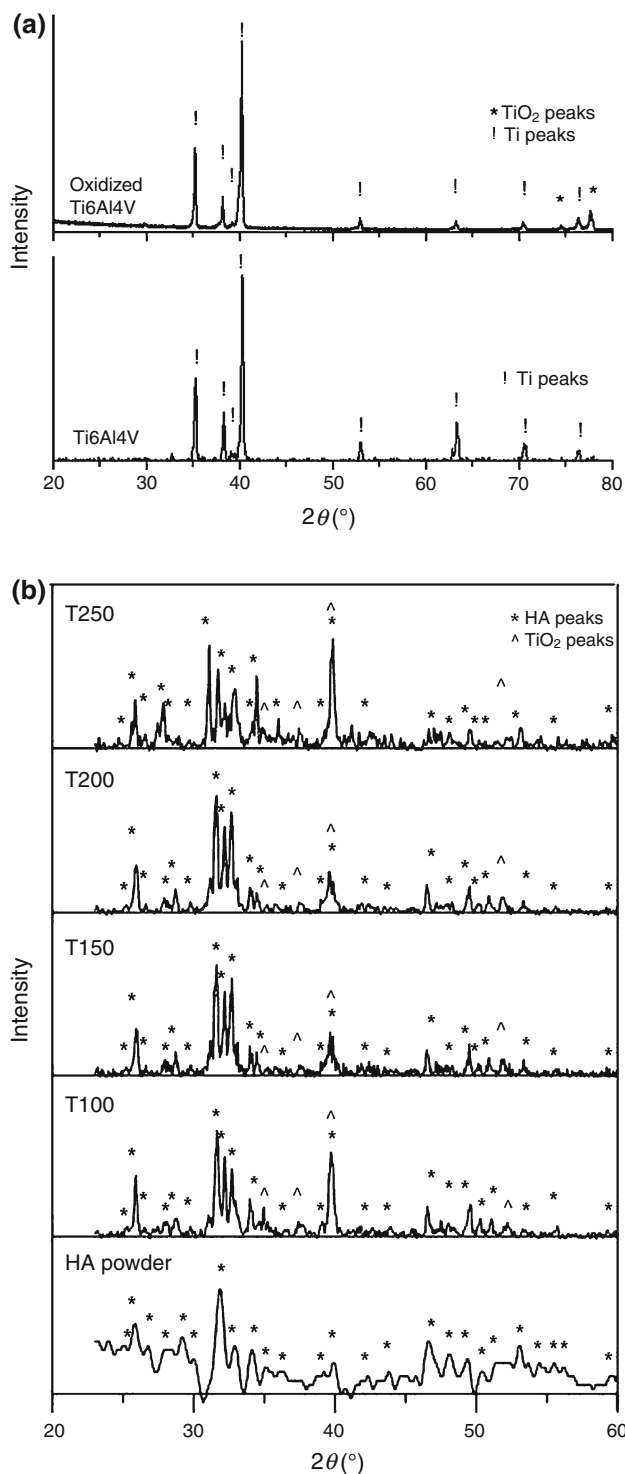
Fig. 2: Comparative chart of X-ray diffraction patterns of (a) Ti6Al4V substrate and thermally grown oxide layer and (b) HA powder, samples T100, T150, T200, and T250

deposited at various voltages. The results support the formation of HA coating on oxidized Ti6Al4V substrate and absence of any other reaction products. Also, we noticed that HA has not decomposed into

β-TCP (β-tri-calcium phosphate) or any other unstable phase during sintering. Crystallite size in the grains of HA coatings was estimated using Scherrer's formula ($t = 0.9\lambda/(B \cos \theta)$) after taking care of the instrumental broadening using an Si standard. The estimated values of crystallite sizes for different samples with varying deposition voltage are shown in Table 1. It is observed that the deposition voltage does not play any major role on the crystallite size of HA, remaining ∼40 nm.

Microstructural characterization

Following the phase analysis, all the four samples were subjected to microscopy studies for microstructural analysis. Figure 3a shows a cross-sectional optical micrograph of a typical coating obtained for the T200 sample. A schematic of the representative cross section of such samples is provided in Fig. 3b. The sample showed uniform and void free coatings. For instance, Fig. 3b shows three layers on the Ti6Al4V substrate which were characterized as thermally grown TiO$_2$ (Fig. 3c), TiO$_2$ grown during EPD and sintering, and the HA layer deposited during EPD and sintering (Fig. 3d). Thermally grown TiO$_2$ layer was also observed by other researchers showing a blue coloration of the surface.[37] Similar layers were found at different voltages and the thermally grown TiO$_2$ layer was found to be about 0.74 μm thick (ranging between 0.68 and 0.80 μm) in all the samples. Since it is the top surface that comes into contact with the biological environment, the microstructural analysis of the surface becomes critical. The following section focuses on the surface morphology that has developed after the EPD and sintering that can allow us to achieve the requisite phase distribution and coverage.

SEM micrographs of HA coated samples deposited at various voltages are shown in Figs. 4, 5, 6, and 7. A first glance suggests a two phase or a biphasic microstructure for the samples T250, T200, T150, and T100, with the size, shape, and distribution of the non-confluent phases varying with the change in the deposition voltage. In all the microstructures, a major phase of HA is noticed, while the second phase is observed to be TiO$_2$ (using electron dispersive spectroscopy technique as shown later in the "Discussion" section). In all of the cases, the primary HA phase contains open microporosity which was uniformly distributed due to the partial sintering of fine (approximately micrometer sized) HA particles at 1000°C for 2 h. A common feature of interconnected particles with substantial porosity (∼21–33%) is evidence of partial sintering of the HA particles. The size of the island in the HA phase varied in the range of 60–96 μm, and the vol.% of the TiO$_2$ phase varied in the range of 17–22% with deposition voltage in the range of 100–250 V (refer to Table 1 for details). Island size of the HA phase and the vol.% of the TiO$_2$ phase were found to decrease while porosity of the HA phase was found to increase with increasing deposition voltage.
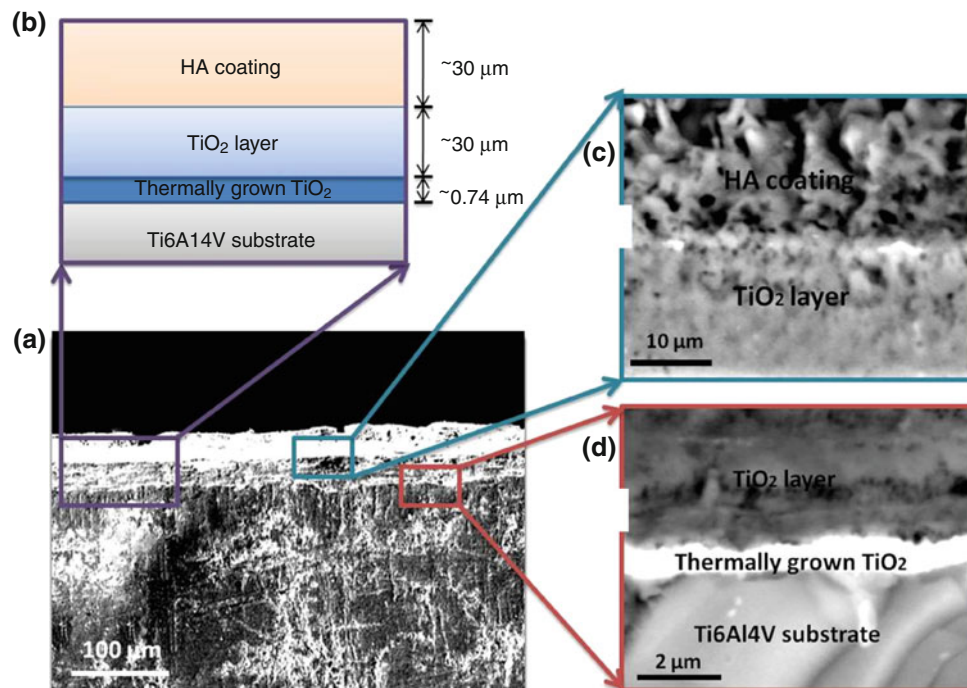
Fig. 3: Cross-sectional SEM image schematic for sample T200 showing multilayered coatings and their magnified image of the interfacial regions. (a) SEM micrograph, (b) schematic with measured thickness, (c) magnified view for thermally grown TiO_2, and (d) HA and TiO_2 boundary
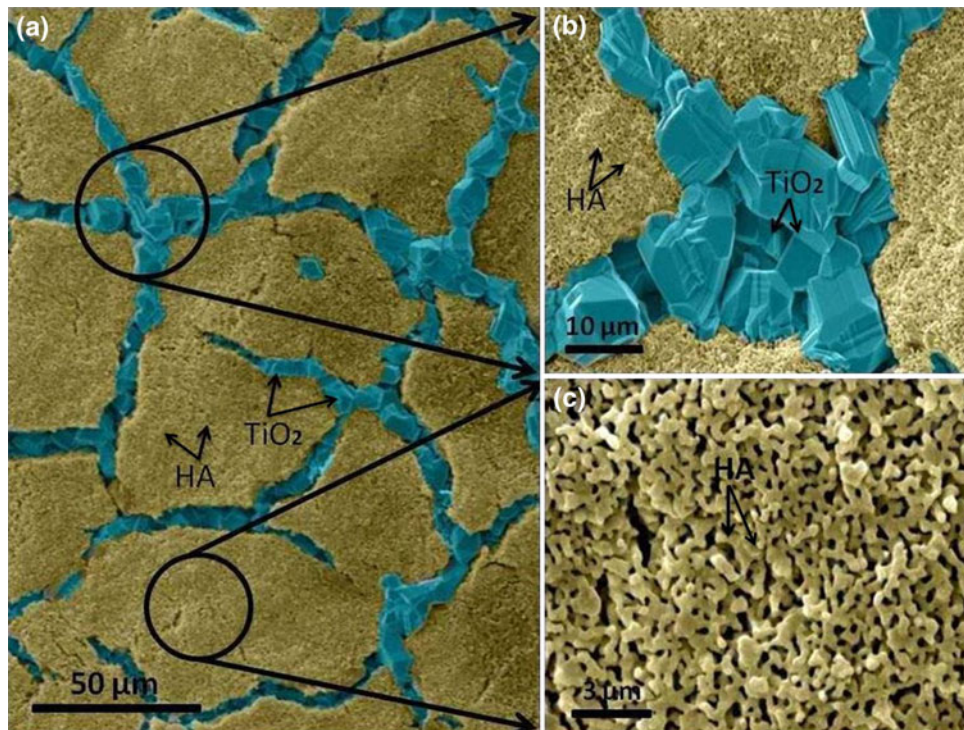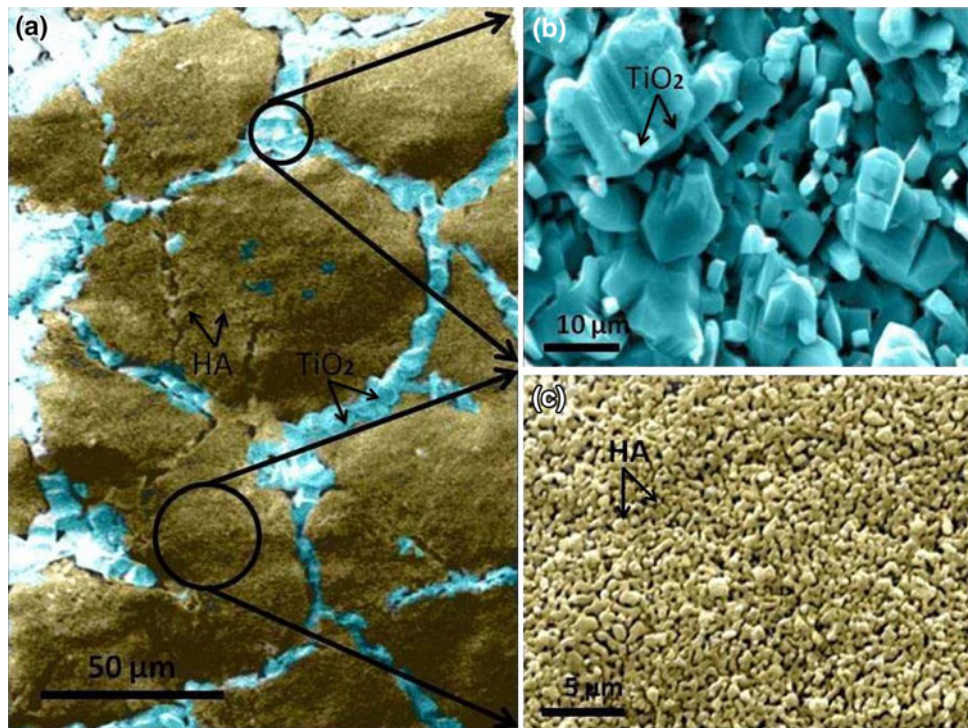

Fig. 4: Schematic of SEM images for sample T250: (a) overall microstructure depicting the presence of two different phases, (b) magnified image of secondary phase TiO_2, and (c) magnified image of primary phase
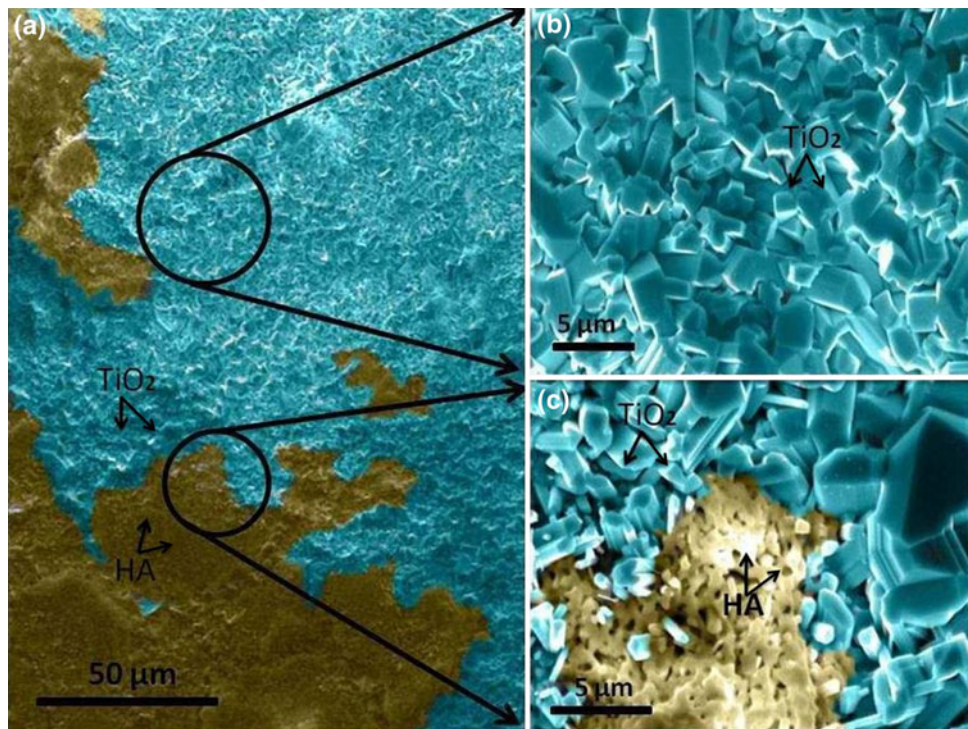
Fig. 5: Schematic of SEM images for sample T200: (a) overall microstructure depicting the presence of two different phases, (b) magnified image of secondary phase TiO_2, and (c) magnified image of primary phase

Fig. 6: Schematic of SEM images for sample T150: (a) overall microstructure depicting the presence of two different phases, (b) magnified image of secondary phase TiO_2, and (c) magnified image of primary phase
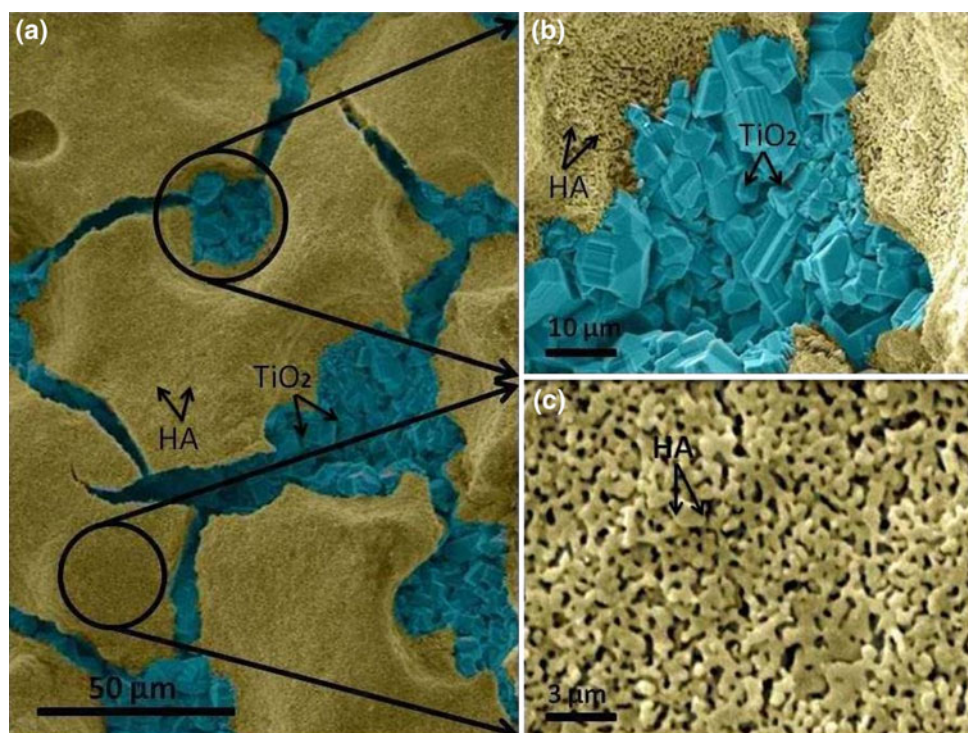
Fig. 7: Schematic of SEM images for sample T100: (a) overall microstructure depicting the presence of two different phases, (b) magnified image of secondary phase TiO$_2$, and (c) magnified image of primary phase

In all of the samples, the TiO$_2$ phase showed dense faceted microstructural features, though the morphology of these feature varied with the deposition voltage. In samples with deposition voltage (100–200 V), the TiO$_2$ phase was found to be irregular polygonal morphology eliciting multiple faces. It can be inferred herein that enhanced nucleation sites at lower deposition voltage resulted in the growth of a large number of individual TiO$_2$ crystals (size of few μm), whereas in sample T250, coalescence of individual features occurred and a single continuous TiO$_2$ phase was found to have commutative growth (showing large particle size of 10–15 μm) along the phase boundaries between HA islands. The line elemental mapping confirmed the presence of the primary HA phase showing calcium and phosphorous peaks (Fig. 7), whereas the secondary phase corresponded to the substrate element peaks (mainly titanium and oxygen with minor peaks of Al and V).

In the T250 sample (Fig. 4), it can be clearly seen that the TiO$_2$ phase is evolving preferentially within the phase boundaries of HA (Fig. 4a). Partially grown TiO$_2$ at this deposition voltage elicits insufficient growth of TiO$_2$, incapable of fully covering the surface, and resulting in the formation of voids (appearing like cracks) during its growth. The morphology of the TiO$_2$ consists of large (~5–25 μm) and dense faceted polycrystalline features with irregular polygonal morphology displaying multiple faces and ridges as shown in Fig. 4b. A single continuous TiO$_2$ phase is observed

due to the coalescence of individual particles. The HA phase was composed of submicron sized coalesced particles as depicted in Fig. 4c. Microstructure of the deposited coating is observed to contain microporosity ~33%, which appears to be interconnected, and is uniformly distributed throughout the surface.

At the deposition voltage of 200 V (sample T200), the TiO$_2$ phase is also evolving preferentially through the boundary of the HA phase as depicted by the biphasic microstructure in Fig. 5a. Well networked distribution of HA and TiO$_2$ suggests that the growth of TiO$_2$ and deposition of HA phase is well integrated since cracking (as observed in T250, Fig. 4) is now circumvented in T200 processing. The morphology of the TiO$_2$ was observed to be consisting of dense but smaller (3–15 μm) faceted polycrystalline features of irregular polygonal morphology having multiple faces and ridges as shown in Fig. 5b. A single continuous TiO$_2$ phase could not be observed due to the insufficient coalescence of individual TiO$_2$ crystals. Uniformly distributed interconnected microporosity (~23–24%) was found in the HA phase as indicated by the porous microstructure containing submicron sized coalesced particles in Fig. 5c.

At the deposition voltage of 150 V (sample T150), the TiO$_2$ phase growth was not limited to the cracks of HA phase, but the biphasic microstructure is elicited as scattered zones of TiO$_2$ within the HA phase (Fig. 6a). The morphology of the TiO$_2$ consisted of dense but finer (0.25–10 μm) faceted polycrystalline features of

irregular polygonal morphology displaying multiple faces and ridges as shown in Fig. 6b. These zones consist of individual and scattered TiO_2 without much integration. Uniformly distributed interconnected microporosity in HA was also observed, as seen in Fig. 6c, confirming the partial sintering of HA.

At the deposition voltage of 100 V (sample T100), the growth of the TiO_2 phase led to the formation of large pits ($\sim$30–60 μm) due to widening of phase boundaries to accommodate higher growth of TiO_2 and confining it preferentially within the phase boundaries of HA phase, as depicted by the biphasic microstructure in Fig. 7a. Widening and pit formation at phase boundaries of HA phase at this deposition voltage resulted due to an excessive growth of TiO_2, which was incapable of accommodating the initial cracking introduced during its growth. Figure 7b shows a highly magnified SEM image of TiO_2 region. The morphology of the TiO_2 was found to consist of dense and fine (0.25–8 μm) faceted polycrystalline features of irregular polygonal morphology showing multiple faces and ridges. Additionally, individual TiO_2 phase was prominent in the phase boundaries and pit regions. Uniformly distributed interconnected microporosity in HA was also found as depicted in Fig. 7c and confirming the partial sintering of HA.

Mechanical characterization

Microhardness estimated by Vickers indentation (model Bareiss Digi) test elicited the bi-modal nature of hardness values, justified by the presence of two phases in the microstructure. The effect of deposition voltage on hardness profile of samples T250, T200, T150, and

Fig. 8: Variation of microhardness with deposition voltage

T100 along with the base hardness of Ti6Al4V is presented in Fig. 8. The bi-modal hardness profile showed high hardness of dense faceted crystalline TiO_2 phase (675–775 H_V) and low hardness of highly porous structure of HA (500–650 H_V). It is observed that an increase in the deposition voltage led to enhanced porosity of HA phase and hence resulted in a decreased hardness. Base hardness of the metallic alloy Ti6Al4V substrate was found to be lower ($\sim$330 H_V) than that of EPD deposited HA coatings. Owing to inherently high hardness of TiO_2 (675–775 H_V, in comparison to that of HA $\sim$500–650 H_V), a very high hardness difference was observed between the HA and TiO_2 phase in samples T100 and T150 ($\sim$up to 250–300 H_V), whereas the hardness difference in samples T200 and T250 was not as great ($\sim$150 H_V).

Discussion

As the microstructure of all the samples showed the presence of two different phases, identification of the two phases present was done by EDX analysis. The elemental mapping on a line crossing the phase boundary and individually on both phases is shown in Fig. 9. The elemental compositions corresponding to both the phases at the boundary region confirm the presence of high Ca, P, and O in the primary phase and high Ti and O in the secondary phase. The regions with high Ca/P/O depict HA (the primary phase) while those with high Ti/O depict TiO_2 (the secondary phase).

Retention of HA after the thermal treatment was confirmed by the TEM characterization done on Sample T200. Multiple crystallites of average size ranging less than 40–50 nm are visible in Fig. 10a corroborating the crystallite size ($\sim$40 nm) as estimated by Scherrer equation from XRD data. Selected area diffraction pattern (SADP) composed of spotted ring pattern confirmed polycrystalline HA with multiple nano-crystals of HA. All the indexed rings matched with various crystallographic planes of HA as shown in Fig. 10b eliciting the retention of HA phase in the coatings after EPD and sintering.

Almost 40-fold growth in TiO_2 layer (from 0.74 to 30 μm) as shown in Fig. 3a does not comply with the idea that the growth of TiO_2 has resulted from the thermal oxidation alone, as thermal oxidation was done only for 2 h (at 600°C) in an inert atmosphere of N_2. Another possible mechanism for such a thick oxide layer formation can be attributed to the anodic oxidation during the EPD of HA in TiO_2 coated Ti6Al4V substrate. However, the TiO_2 that evolved in the present work differs from the previous observation of vertical growth of TiO_2 nanotubes during anodic oxidation.[38–40] Since faceted crystalline growth of TiO_2 is evident from the morphology of the grown structures in the present work, it does not comply with its evolution from anodic oxidation alone. This indicates that the modification of TiO_2 has occurred to form
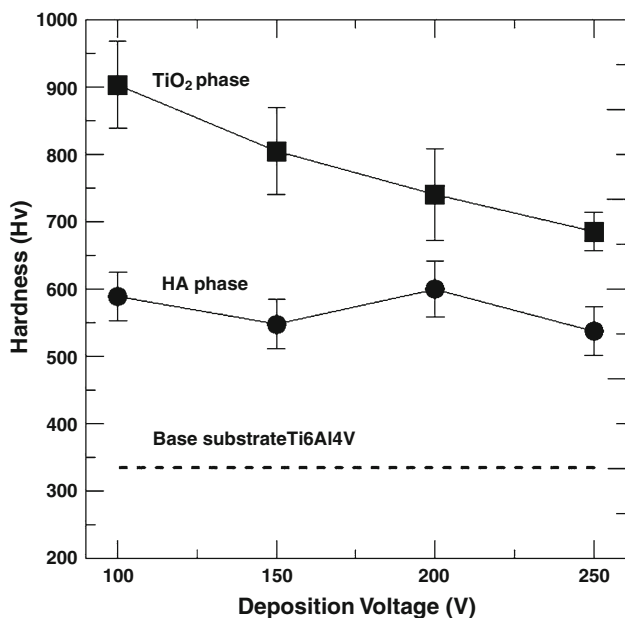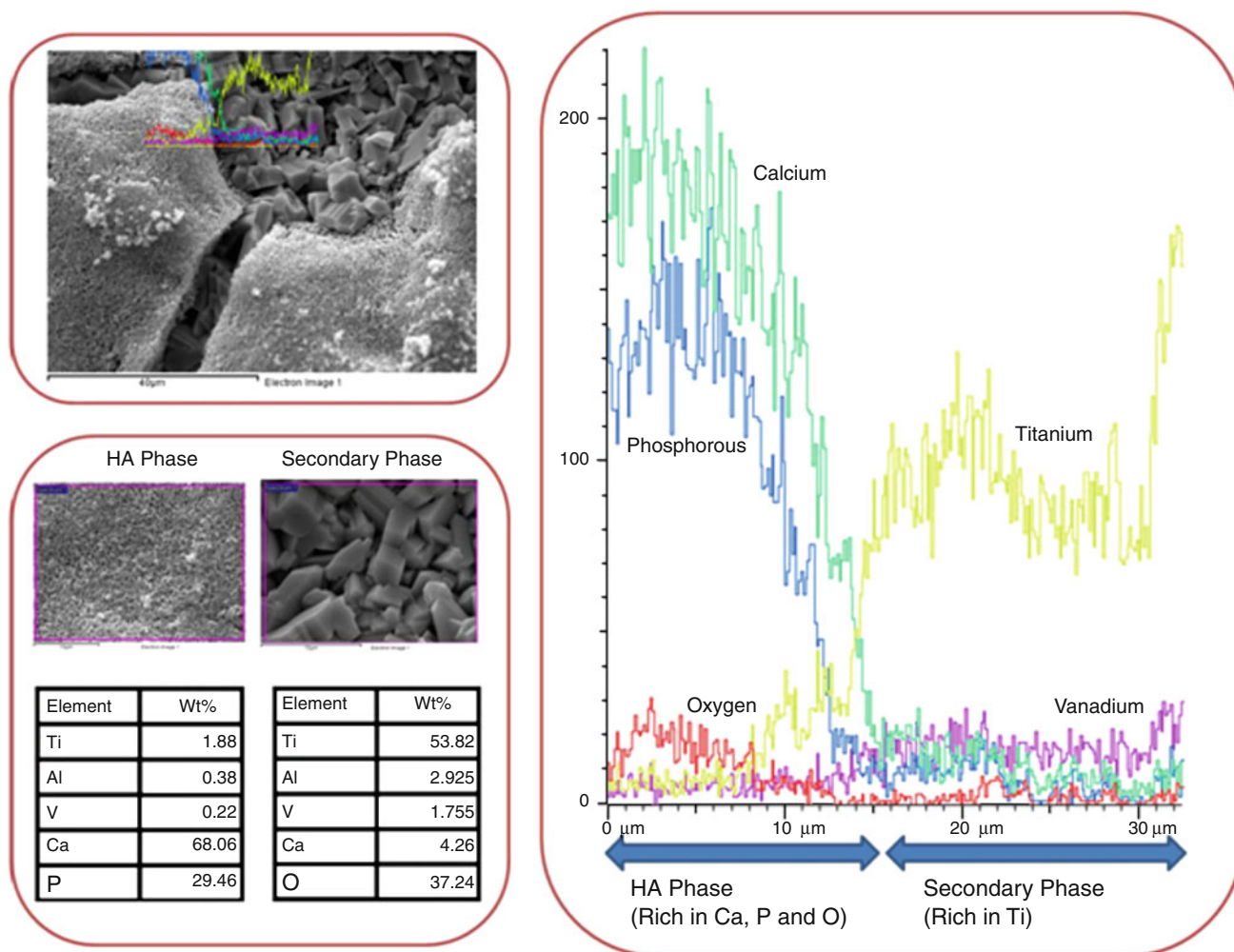
Fig. 9: EDX on sample T200 for elemental mapping on a line crossing the boundary and individually on both primary and secondary phase

faceted crystals, which is attributed to the prolonged high temperatures sintering (at 1000°C for 2 h) after EPD. Such a transition of TiO_2 morphology matches with the past observations during thermal growth of thin TiO_2 coatings over Ti wires.[41] The formation of these 3-D faceted morphological structures can be explained through the growth of polycrystalline TiO_2 film in different morphological motifs arising from the difference in the Gibbs free energy of the cylinder and plate like structure of TiO_2.[41]

$$\frac{\Gamma \text{ cylinder}}{\Gamma \text{ plate}} \gg 1,$$

where Γ cylinder denotes the interfacial Gibbs free energy of the cylindrical geometry crystals and Γ plate denotes the interfacial Gibbs free energy of the cylindrical geometry crystals. It is believed that TiO_2 undergoes self-reconstitution and reorganization on the microscopic level during the sintering operation in

order to lower its free energy.[41] Such a mechanism of microstructural adjustment in TiO_2 is manifested by the presence of stacked layers in the ridges, and not of cylindrical nanotubes of TiO_2 as shown in Fig. 11.

The initial TiO_2 layer thickness is 0.74 μm after the thermal oxidation at 600°C for 2 h. It must be mentioned that TiO_2 growth occurs first due to anodic oxidation during the EPD duration (10 s) followed by a second stage of growth during sintering at 1000°C for 2 h. Though the presence of intermediate TiO_2 layer is expected to stop or alleviate the interfacial reaction between the metal and the ceramic interface, in fact, it has led to a dramatic growth (~40 times) resulting in enhanced penetration through the HA layer deposited on top of it. Thus, it can be concluded that the EPD of HA and anodic oxidation of TiO_2 have occurred simultaneously during the 10 s cycle of the applied voltage field utilized in the current work. Further, the growth kinetics of HA and TiO_2 both depend on the applied voltage eliciting the microstructural differences achieved with voltage variation. In the present work, the
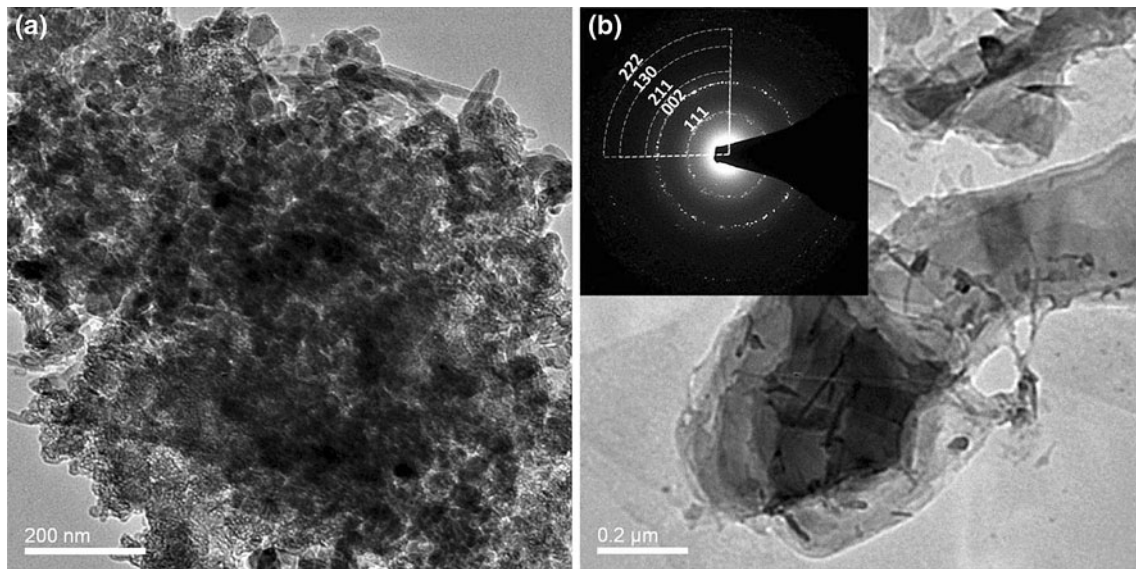
Fig. 10: Schematic of TEM images of the scratched HA coating from the sample T200 (a) displaying nano crystallites (b) magnified image with the indexed SADP image in the onset
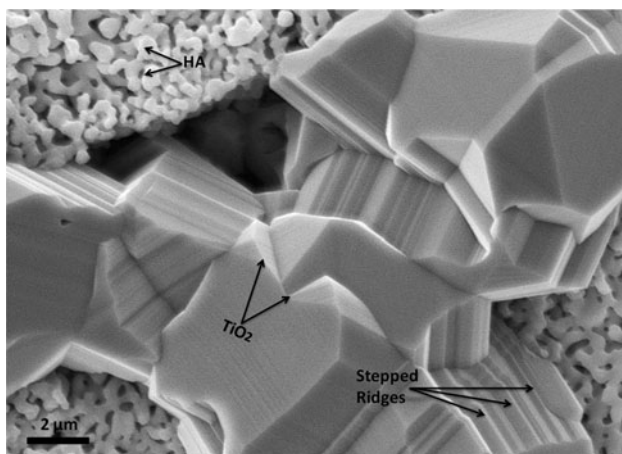

Fig. 11: High magnification SEM image showing stacked layers due to ridge formation during sintering at 1000°C for 2 h

thickness of the coating is in the micrometer range and the distance between the electrodes was set to be 5 cm (as stated in the ''Electrophoretic deposition (EPD)'' section). Hence, keeping in mind the large difference between d and d_{deposit}, the term d_{deposit} can easily be neglected from $(d - d_{\text{deposit}})$ and that leaves us with the approximate kinetic equation of weight deposited (w) of HA during EPD with only the term 'd' in it[42]:

$$w = \left(\frac{2}{3}\right) f C \varepsilon_{\text{o}} \varepsilon_{\text{r}} \xi \left(\frac{1}{\eta}\right) \left(\frac{V_{\text{applied}}}{d}\right) t$$

where all the parameters, deposit factor (f), particle concentration in suspension (C), permittivity of vacuum (ε_{o}), relative permittivity (ε_{r}), zeta potential (ξ), deposition time (t), distance between the electrodes

(d), and viscosity of solvent (η) are kept fixed for the four samples with varying applied voltage (V_{applied}).

As a result, the above equation can be reduced to a linear equation:

$$w = K V_{\text{applied}}$$

where K is an overall constant and weight deposited electrophoretically has a direct linear dependence on the deposition voltage. TiO_2 evolution, on the other hand, follows an equation comprising many factors associated with hydrogen gas evolution, anodic current, deposition voltage, etc. Since all other variables are constant for the four samples, the evolution kinetics of TiO_2 crystals depends only on the voltage. Thus, while higher voltage promotes EPD of HA, it also promotes TiO_2 growth simultaneously via anodic oxidation.

The two parallel growth processes of HA and TiO_2 are both favored by the increasing deposition voltage as suggested by the kinetics of EPD and anodic oxidation. Still, the trend of the competing kinetics of both the processes can be observed by the topography of HA and TiO_2 on the coating surface. The schematic diagram in Fig. 12 shows a representation of the effect of voltage on the evolution of TiO_2 phase and its distribution at the coating surface. The micrograph for sample T250 (Fig. 4) shows that the faceted features of TiO_2 are above the surface of HA phase, while sample T100 (Fig. 7) shows that the faceted features of TiO_2 are below the level of surface of HA phase. These unleveled topographical features were not observed between the surfaces of TiO_2 and HA, as seen in T200 (Fig. 5) and T150 (Fig. 6). Thus, an enhanced integrity of coatings can be expected in T200 and T150 in comparison to those of T250 and T100 samples.
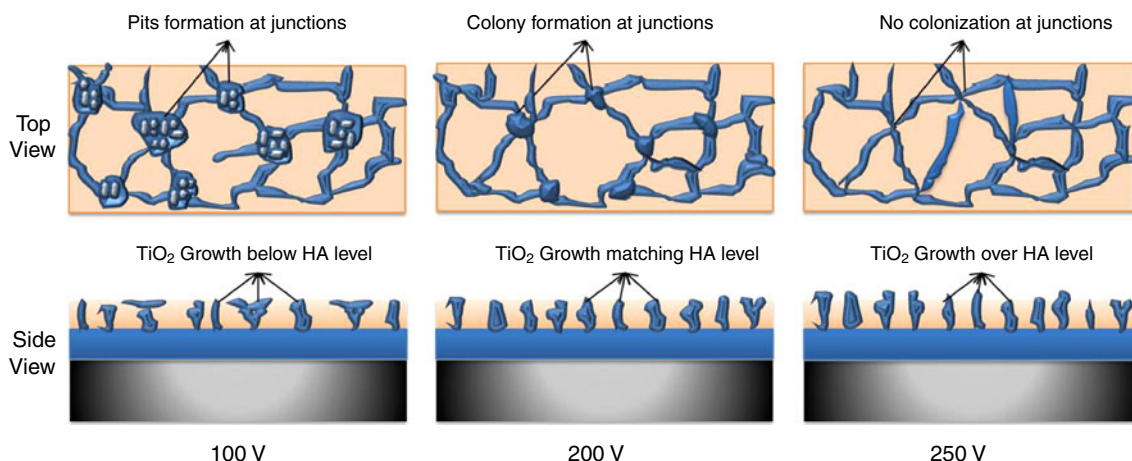
Fig. 12: Schematic of the probable/proposed mechanism for the evolution of the TiO$_2$ phase with variation in deposition voltage

Deposition at higher voltages also leads to increased tendency of coalescence of the individual particles (eliciting bigger particle size), and a continuous TiO$_2$ phase distribution in HA phase (i.e., 5–25 μm in T250, 3–15 μm in T200 sample), a much lesser extent of coalescence of TiO$_2$ particles is observed in sample T150 (0.25–10 μm) and T100 (0.25–8 μm), in contrast to those of sintered coatings deposited at higher voltages. Hence, the comparative growth between HA and TiO$_2$ indicates that higher voltage supports TiO$_2$ growth when compared to that of HA deposition. In contrast, with decreasing deposition voltage, widening of HA phase boundary and formation of pits were observed.

Accommodation of TiO$_2$ at the island boundary of HA, and thus its prevention from cracking appears to optimize for T150 and T200 V. Higher voltage assists comparatively higher deposition of TiO$_2$, in contrast to that of HA (as seen in Figs. 4, 5, 6, 7). With decreasing deposition voltage, HA grows preferentially leaving the remaining space as voids. As a result, a larger island with wider cracks (or voids) is observed. On the other hand, at higher voltages, TiO$_2$ growth competes with that of HA resulting in smaller HA island size. Thus, lower voltage resulted in larger island size as supported by the data (increasing from 60 μm at 250 V to 96.1 μm at 100 V), and as shown in Fig. 13. On the other hand, porosity content in HA phase was found to increase with the deposition voltage. Such a trend was expected since rapid deposition rate at higher voltage[42] allows limited time for particle rearrangement leading to higher porosities (increasing from 21.6% at 100 V to 33.0% at 250 V) as shown in Fig. 13.

Since the samples are sintered at high temperature (1000°C, 2 h) and experience similar thermal treatment, the difference in the morphology and distribution of phases can be attributed to the EPD voltage alone.
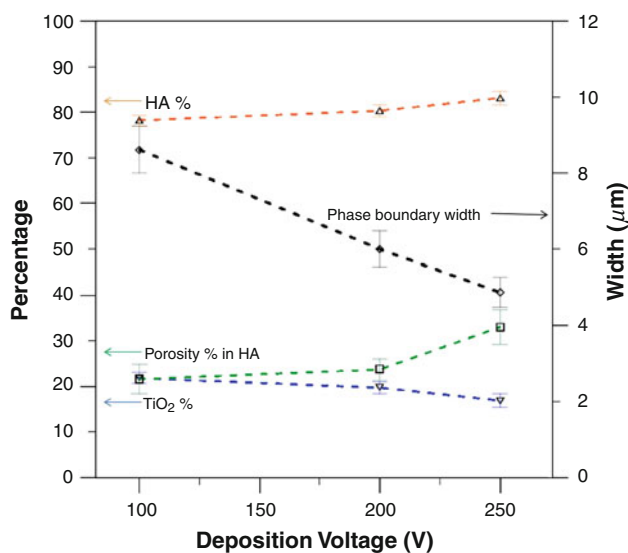

Fig. 13: Variation of phase boundaries width, porosity % in HA, HA% and TiO$_2$% in top surface with change in deposition voltage

Overall, the deposition voltage affects various characteristics of the coating: phase distribution at the surface, integration of TiO$_2$ features, minimization of cracks, and physical property match between HA–TiO$_2$. Among all the samples, T200 appears to be the most promising considering the comparative distribution of HA–TiO$_2$, sufficient integration of the TiO$_2$ features, and closest mechanical property (hardness) match between HA–TiO$_2$ (see Fig. 8). As TiO$_2$ is known for its antibacterial properties, further work on the bioactivity and antibacterial property needs to be carried out to investigate the role of phase distribution on the bactericidal nature of deposited coatings.

Conclusions

Successful EPD of hydroxyapatite (over deposition voltage of 100–250 V) was achieved on Ti6Al4V substrate with thermally grown TiO_2 layer (0.74 μm thick grown at 600°C for 2 h). Biphasic microstructure was observed showing faceted morphology of TiO_2 within the phase boundary of HA islands. Porosity in HA, island size of HA, and distribution of dense faceted TiO_2 structures showed a strong dependence on the deposition voltage. In parallel to the EPD of HA, anodic oxidation of substrate was also confirmed by occurrence of dense faceted crystalline TiO_2. Such faceted morphology of TiO_2 crystals was attributed to the lowering of free energy of formation of stacked plate-like TiO_2 during prolonged high temperature sintering (1000°C, 2 h). Further evaluation of cyto-compatibility, role of TiO_2 dispersion on bactericidal effects, and tribological response of electrophoretically deposited coatings will be needed for their utilization as potential biomaterials.

References

1. Santavirta, S, et al., "Biocompatibility of Hydroxyapatite-Coated Hip Prostheses." *Arch. Orthop. Trauma Surg.*, **110** 288–292 (1991)

2. Labella, R, Braden, M, Debt, S, "Novel Hydroxyapatite-Based Dental Composites." *Biomaterials*, **15** (15) 1197–1200 (1994)

3. Paital, SR, Dahotre, NB, "Calcium Phosphate Coatings for Bio-implant Applications: Materials, Performance Factors, and Methodologies." *Mater. Sci. Eng., R*, **66** 1–70 (2009)

4. Aksakal, B, Hanyaloglu, C, "Bioceramic Dip Coating on Ti-6Al-4V and 316L SS Implant Materials." *J. Mater. Sci. Mater. Med.*, **19** (5) 2097–2104 (2008)

5. Haslauer, CM, et al., "In Vitro Biocompatibility of Titanium Alloy Discs made Using Direct Metal Fabrication." *Med. Eng. Phys.*, **32** 645–652 (2010)

6. Hayashi, K, et al., "Evaluation of Metal Implants Coated with Several Types of Ceramics As Biomaterials." *J. Biomed. Mater. Res.*, **23** (11) 1247–1259 (1989)

7. Grecu, M, et al., "Enhancing the Performance of Titanium Surface Via Elaboration of a Nanostructure and a Bioactive Coating." *Universitatea Politehnica Bucuresti Scientific Bulletin Series B*, **74** (2) 113–127 (2012)

8. Kalmodia, S, et al., "Microstructure, Mechanical Properties and In Vitro Biocompatibility of Spark Plasma Sintered Hydroxyapatite-Aluminum Oxide-Carbon Nanotube Composite." *Mater. Sci. Eng., C*, **30** (8) 1162–1169 (2010)

9. Balani, K, et al., "Plasma-Sprayed Carbon Nanotube Reinforced Hydroxyapatite Coatings and their Interaction with Human Osteoblasts In Vitro." *Biomaterials*, **28** 618–624 (2007)

10. Balani, K, et al., "Tribological Behavior of Plasma Sprayed Carbon Nanotube Reinforced Hydroxyapatite-Coating in Physiological Solution." *Acta Biomater.*, **3** (6) 944–951 (2007)

11. de Sena, L, et al., "Hydroxypatite Deposition by Electrophoresis on Titanium Sheets with Different Surface Finishing." *J. Biomed. Mater. Res.*, **60** 1–7 (2002)

12. Ma, J, Wang, C, Peng, KW, "Electrophoretic Deposition of Porous Hydroxyapatite Scaffold." *Biomaterials*, **24** 3505–3510 (2003)

13. Nie, X, Leyland, A, Matthews, A, "Deposition of Layered Bioceramic Hydroxyapatite/TiO_2 Coatings on Titanium Alloys Using a Hybrid Technique of Micro-arc Oxidation and Electrophoresis." *Surf. Coat. Technol.*, **125** 407–414 (2000)

14. Ducheyne, P, et al., "Calcium Phosphate Ceramic Coatings on Porous Titanium: Effect of Structure and Composition on Electrophoretic Deposition, Vacuum Sintering and In Vitro Dissolution." *Biomaterials*, **11** 244–254 (1990)

15. Manso, M, et al., "Electrodeposition of Hydroxyapatite Coatings in Basic Conditions." *Biomaterials*, **21** 1755–1761 (2000)

16. Mavis, B, Tas, AC, "Dip Coating of Calcium Hydroxyapatite on Ti-6Al-4V Substrates." *J. Am. Ceram. Soc.*, **83** 989–991 (2000)

17. García-Sanz, FJ, et al., "Hydroxyapatite Coatings: A Comparative Study Between Plasma-Spray and Pulsed Laser Deposition Techniques." *J. Mater. Sci. Mater. Med.*, **8** 861–865 (1997)

18. Tercero, JE, et al., "Effect of Carbon Nanotube and Aluminum Oxide Addition on Plasma-Sprayed Hydroxyapatite Coating's Mechanical Properties and Biocompatibility." *Mater. Sci. Eng., C*, **29** 2195–2202 (2009)

19. Montenero, A, et al., "Sol–Gel Derived Hydroxyapatite Coatings on Titanium Substrate." *J. Mater. Sci.*, **35** (11) 2791–2797 (2000)

20. Li, P, Groot, Kd, Kokubo, T, "Bioactive $Ca_{10}(PO_4)_6(OH)_2$-TiO_2 Composite Coating Prepared by Sol–Gel Process." *J. Sol-Gel Sci. Technol.*, **7** 27–34 (1996)

21. Oshida, Y, *Bioscience and Bioengineering of Titanium Materials*. Elsevier, Amsterdam, 2007

22. Leon, B, Jansen, J, *Thin Calcium Phosphate Coatings for Medical Implants*, p. 356. Springer-Verlag, New York, 2009

23. Basu, RN, Randall, CA, Mayo, MJ, "Fabrication of Dense Zirconia Electrolyte Films for Tubular Solid Oxide Fuel Cells by Electrophoretic Deposition." *J. Am. Ceram. Soc.*, **84** (1) 33–40 (2001)

24. Zhang, YY, et al., "Electrochemical Deposition of Hydroxyapatite Coatings on Titanium." *Trans. Nonferrous Met. Soc. China*, **16** (3) 633–637 (2006)

25. Wang, YC, Leu, IC, Hon, MH, "Kinetics of Electrophoretic Deposition for Nanocrystalline Zinc Oxide Coatings." *J. Am. Ceram. Soc.*, **87** 84–88 (2004)

26. Ruys, AJ, et al., "Sintering Effects on the Strength Hydroxyapatite." *Biomaterials*, **16** 409–415 (1995)

27. Wei, M, Evans, JH, Wentrup-Byrne, E, "Decomposition of Dual Hydroxyapatite/Fluorapatite Coatings on Metal Substrates." *J. Aust. Ceram. Soc.*, **36** (1) 47–52 (2000)

28. Wei, M, et al., "Hydroxyapatite-Coated Metals: Interfacial Reactions During Sintering." *J. Mater. Sci. Mater. Med.*, **16** 101–106 (2005)

29. Wei, M, et al., "Electrophoretic Deposition of Hydroxyapatite Coatings on Metal Substrates: A Nanoparticulate Dual-Coating Approach." *J. Sol-Gel Sci. Technol.*, **21** (1/2) 39–48 (2001)

30. Albayraka, O, El-Atwani, O, Altintas, S, "Hydroxyapatite Coating on Titanium Substrate by Electrophoretic Deposition Method: Effects of Titanium Dioxide Inner Layer on

Adhesion Strength and Hydroxyapatite Decomposition." *Surf. Coat. Technol.*, **202** 2482–2487 (2007)

31. Nie, X, et al., "Effects of Solution pH and Electrical Parameters on Hydroxyapatite Coatings Deposited by a Plasma-Assisted Electrophoresis Technique." *J. Biomed. Mater. Res.*, **57** 612–618 (2001)

32. Kumar, RR, Wang, M, "Functionally Graded Bioactive Coatings of Hydroxyapatite/Titanium Oxide Composite System." *Mater. Lett.*, **55** 133–137 (2002)

33. Karpagavalli, R, et al., "Corrosion Behavior and Biocompatibility of Nanostructured TiO_2 Film on Ti6Al4V." *J. Biomed. Mater. Res., Part A*, **83A** (4) 1087–1095 (2007)

34. Cui, C, et al., "Fabrication and Biocompatibility of Nano-TiO_2/Titanium Alloys Biomaterials." *Mater. Lett.*, **59** 3144–3148 (2005)

35. Mondragon-Cortez, P, Vargas-Gutierrez, G, "Electrophoretic Deposition of Hydroxyapatite Submicron Particles at High Voltages." *Mater. Lett.*, **58** 1336–1339 (2004)

36. Meng, X, et al., "Effects of Applied Voltages on Hydroxyapatite Coating of Titanium by Electrophoretic Deposition." *J. Biomed. Mater. Res. B Appl. Biomater.*, **78** 373–377 (2006)

37. Dubey, M, et al., "TiO_2 Nanotube Membranes on Transparent Conducting Glass For High Efficiency Dye-Sensitized Solar Cells." *Nanotechnology*, **22** (28) 285201.1–285201.9 (2011)

38. Wang, N, et al., "Evaluation of Bias Potential Enhanced Photocatalytic Degradation of 4-Chlorophenol with TiO_2 Nanotube Fabricated by Anodic Oxidation Method." *Chem. Eng. J.*, **146** 30–35 (2009)

39. Yue-qin, W, et al., "HA Coating on Titanium with Nano-tubular Anodized TiO_2 Intermediate Layer via Electrochemical Deposition." *Trans. Nonferrous Met. Soc. China*, **18** 631–635 (2008)

40. Park, HH, et al., "Bioactive and Electrochemical Characterization of TiO_2 Nanotubes on Titanium via Anodic Oxidation." *Electrochim. Acta*, **55** (20) 6109–6114 (2010)

41. Azad, AM, "Gas Phase Nanofication: A Strategy to Impart Fast Response in Sensors." In: Ahmed, W, Jackson, MJ (eds.) *Emerging Nanotechnologies for Manufacturing*, pp. 17–57. William Andrew Publishers/Academic Press, New York, 2009

42. Ciou, S-J, Fung, K-Z, Chiang, K-W, "The Mathematical Expression for Kinetics of Electrophoretic Deposition and the Effects of Applied Voltage." *J. Power Sources*, **172** 358–362 (2007)